THEMATIC SECTION: ADDITIVE MANUFACTURING BENCHMARKS 2022

Phase Composition and Phase Transformation of Additively Manufactured Nickel Alloy 718 AM Bench Artifacts

Fan Zhang[1] · Aaron C. Johnston-Peck[1] · Lyle E. Levine[1] · Michael B. Katz[1] · Kil-Won Moon[1] · Maureen E. Williams[1] · Sandra W. Young[1] · Andrew J. Allen[1] · Olaf Borkiewicz[2] · Jan Ilavsky[2]

Abstract

Additive manufacturing (AM) technologies offer unprecedented design flexibility but are limited by a lack of understanding of the material microstructure formed under their extreme and transient processing conditions and its subsequent transformation during post-build processing. As part of the 2022 AM Bench Challenge, sponsored by the National Institute of Standards and Technology, this study focuses on the phase composition and phase evolution of AM nickel alloy 718, a nickel-based superalloy, to provide benchmark data essential for the validation of computational models for microstructural predictions. We employed high-energy synchrotron X-ray diffraction, in situ synchrotron X-ray scattering, as well as high-resolution transmission electron microscopy for our analyses. The study uncovers critical aspects of the microstructure in its as-built state, its transformation during homogenization, and its phase evolution during subsequent aging heat treatment. Specifically, we identified secondary phases, monitored the dissolution and coarsening of microstructural elements, and observed the formation and stability of γ' and γ'' phases. The results provide the rigorous benchmark data required to understand the atomic and microstructural transformations of AM nickel alloy 718, thereby enhancing the reliability and applicability of AM models for predicting phase evolution and mechanical properties.

Introduction

Additive manufacturing (AM) represents one of the most promising advanced manufacturing technologies. As the continuation of the digital revolution in the manufacturing domain, it improves design flexibility, reduces the duration of product engineering and production cycles, and impacts materials sustainability through reduced waste. Since its inception, AM, especially AM of metals, has found numerous applications across industries ranging from aerospace, defense, and healthcare to energy.

In a typical AM build process, a high-powered heat source, such as a laser or electron beam, interacts with the feedstock material according to a prescribed digital model. The interaction between the heat source and the feedstock is typically transient, resulting in extreme processing conditions where the cooling rate often exceeds 1×10^5 °C/s. Such extreme and non-equilibrium processing conditions present significant challenges for understanding the formation pathway of the microstructure and the material's response to the post-built treatments, which in turn affects the AM product's consistency and certifiability.

In addition to the extreme processing conditions, the parameter space of the AM processing is immense, adding to the challenges. Variables such as laser power, laser spot size, scan speed, hatch spacing, layer thickness, scan pattern, substrate temperature, gas flow, and materials properties all contribute to the AM process' outcome. The vast parameter space makes relying on conventional trial-and-error approaches for process development and optimization impractical. Computational models, especially multi-physics

✉ Fan Zhang
   fan.zhang@nist.gov

[1] Material Measurement Laboratory, National Institute of Standards and Technology, Gaithersburg, MD 20899, USA

[2] X-ray Science Division, Argonne National Laboratory, Lemont, IL 60439, USA

models that incorporate key aspects of AM processing, have a unique role in advancing and maturing AM technologies [1]. By simulating the thermal, mechanical, and material phenomena during the AM and post-build processes, these models provide valuable insights into the interplay between various parameters and the end product, hence offering a cost-effective path to accelerate the widespread industrial adoption of AM technologies.

The crucial role of modeling in the AM's advancement requires rigorous and well-defined benchmarks. Based on this need, the U.S. Department of Commerce's National Institute of Standards and Technology initiated an Additive Manufacturing Benchmark Test Series (AM-Bench) that aims to provide the AM modeling community the critically needed, high-pedigree experimental data to facilitate AM standardization, model validation, regulatory compliance, and industry adoption [2, 3]. This triennial series, released twice already (in 2018 and pandemic-delayed 2022), has provided comprehensive sets of experimental data covering a broad range of AM processes and product characteristics. These data provide a common platform for researchers worldwide to assess the accuracy and reliability of their models.

For metallic materials, the microstructure significantly influences the materials' mechanical properties and overall performance. However, the departure of AM's processing conditions from more conventional manufacturing methods, such as casting or wrought, can lead to unusual microstructural features. These features include, severe elemental microsegregation [4], columnar grain structure [5], unexpected phases [6], and unexpected phase evolution sequence [7].

Phase composition and phase evolution are essential elements of a metallic material's microstructural development. In AM materials, previous studies have demonstrated unexpected behaviors in phase composition and phase evolution, both during the AM process and in post-build heat treatment. Modeling these aspects of AM microstructures remains a significant challenge [8]. This is primarily due to difficulties in predicting the formation of metastable phases and phase evolution under the highly non-equilibrium conditions of AM using classical phase transformation models. Additionally, modeling phase composition and phase evolution in AM is inherently multiscale, which adds to its complexity and computational cost.

For these reasons, phase composition and phase evolution measurements have been central elements in both iterations of AM Bench. In AM Bench 2018, our focus was on the phases and phase evolutions of AM 15-5 precipitation-hardenable stainless steel and the nickel-based superalloy 625 [9]. In AM-Bench 2022, our primary effort shifted to the AM nickel-based superalloy 718 (referred to henceforth as 718). Unlike 625, which is designed as a single-phase alloy, 718 is precipitation-hardenable and involves the formation of γ' and γ'' precipitates during heat treatment, adding further complexity. In this work, we will provide detailed information on the fabrication and preparation of AM samples, as well as measurements and results for the following challenge:

- Phase Evolution (CHAL-AMB2022-01-PE): Formation and evolution of phases and phase fractions, including major precipitates, as a function of time for heat treatments of 718 from a 2.5 mm leg (the definition of "leg" in this context is explained later in section "Materials").

Through this challenge, we aim to present comprehensive data on the atomic structure and microstructure of AM 718. Such information is crucial for establishing the structure–property-performance relationships of AM materials at the most fundamental level. These data serve as a foundation for rigorous AM models that seek to understand how AM materials respond to either the AM process or post-build heat treatments.

Our results are primarily obtained using high-energy synchrotron X-ray diffraction and high-resolution transmission electron microscopy (TEM). These state-of-the-art techniques, which operate at vastly different length scales, and therefore probing different sample volumes, offer both microscopic and bulk perspectives on AM 718's atomic structure and microstructure. In particular, we conducted in situ high-energy X-ray scattering measurements to directly observe structural transformations under a prescribed heat treatment protocol, thereby providing the much-needed time-resolved benchmark data for validating model predictions.

Materials and Methods

Materials

All parts for AM Bench 2022 were fabricated using 718 powders from the same batch. These powders were processed on the NIST Additive Manufacturing Metrology Testbed (AMMT) [10], a laser powder bed fusion (LPBF) platform designed and built by NIST. The certified composition of the 718 powder, as well as its allowable composition range, is provided in Table 1. The particle size distribution (PSD) of the powder was determined at NIST, following the methods outlined in Sect. 7.1.2 of ASTM Standard B215-15, and is documented in Table 2. Prior to each build, the powders were stored in sealed containers, and only virgin powders were used.

The build was conducted on a 718 build plate. Thermocouples monitored the build plate temperature, which

Table 1 Measured composition of the 718 feedstock powders used in this study, alongside the allowable composition range for 718

	Measured (mass fraction)	Standard range (mass fraction)
Ni	53.48%	50.00–55.00%
Cr	18.40%	17.00–21.00%
Fe	Balance	Balance
Nb	5.48%	4.75–5.50%
Mo	3.01%	2.80–3.30%
Ti	1.00%	0.65–1.15%
Al	0.48%	0.20–0.80%
Co	0.02%	1.00 max
Cu	<0.01%	0.30 max
Mn	<0.01%	0.35 max
Si	0.03%	0.35 max
C	0.05%	0.08 max
S	<0.005%	0.015 max
P	<0.01%	0.015 max
B	0.003	0.006 max
Ta	<0.01%	
Ag	<0.0001%	
Pd	<0.0001%	
Se	<0.0001%	
Bi	<0.00003%	
O	0.014	

The elemental compositions were determined using various ASTM methods: ASTM E1479 (Inductively Coupled Plasma Atomic Emission Spectroscopy) for most elements, ASTM E1019 (Combustion Method) for Carbon (C) and Sulfur (S), ASTM E1019 (Fusion Method) for Oxygen (O), Nitrogen (N), and Hydrogen (H), and ASTM E1184 for Bismuth (Bi), Palladium (Pd), Selenium (Se), and Silver (Ag)

Table 2 Particle size distribution of the 718 feedstock powders used in this study, represented by the average of three repeated measurements

Particle size distribution	Vendor (μm)	NIST (μm)
D_{10}	17.53	16
D_{50}	31.98	27
D_{90}	53.79	46

The D10, D50, and D90 values signify the particle sizes below which 10%, 50%, and 90% of the powder mass is contained, respectively. Vendor-supplied measurements were conducted using sieve analysis in accordance with ASTM B214, while NIST measurements were obtained using a commercial dynamic imaging analysis instrument

remained consistently below 86 °C throughout the build process. A continuous-wave (CW) ytterbium fiber (Yb: fiber) laser with a central wavelength of 1070 nm was employed during the build. The laser parameters were set at 285 W for power, 960 mm/s for speed, and 77 μm D4σ for spot size. Here, the laser was assumed to have a Gaussian profile and D4σ represents the width of the Gaussian laser beam distribution where the laser's intensity drops to $\approx 1/e^2$ of its peak value. The hatch spacing was 110 μm, and the nominal layer thickness was 40 μm. A linear hatching scan pattern was used, with a 90° rotation between subsequent layers. High-purity argon was circulated through the build chamber at a flow rate of 390 L/min, and the maximum oxygen level was measured to be below 1000 ppm.

For the AM Bench 2022 challenge, we utilized a bridge structure as depicted in Fig. 1. This structure features 12 legs (L) with varying dimensions: 5 mm (L1, L3, L7), 2.5 mm (L3, L6, L9, L12), and 0.5 mm (L2, L5, L8, L11). Additionally, it includes a unique hollow leg, L10, with internal thin walls. These legs exhibit different thermal histories due to their size variations, thereby affecting their microstructure. In situ thermography was employed to monitor the thermal histories of legs 8 through 10. Further details about the build are available elsewhere [11].

To prepare the samples for microstructure characterization, we employed electrical discharge machining (EDM) to cut the legs from the main bridge structure that was not subject to a stress-relief heat treatment to preserve the as-built microstructure. For the scope of this study, only samples from the 2.5 mm legs were analyzed. Post-EDM, these samples were taken from near the central region of the 2.5 mm legs, specifically along the X–Y plane. This sampling strategy aimed to minimize the influence of thermal effects, such as the heat-affected zone, melting, and evaporation, as well as residual stress induced by the EDM process.

Two types of samples were assessed for the AM Bench 2022 challenge: as-built and heat-treated specimens. An initial EDM cut was made for the heat-treated specimens, followed by ultrasonic cleaning in baths of ethanol and acetone to eliminate surface contaminants. To mitigate oxidation, these cleaned samples were sealed in quartz ampules, evacuated, and backfilled with argon. These sealed ampules were placed into a tube furnace preheated to the target temperature. The timing for the heat treatment started when the furnace temperature stabilized back to the predetermined level, usually within a five-minute window.

After the specified heat treatment duration, the encapsulated samples were promptly removed and submerged in room-temperature water without breaking the ampule to facilitate rapid cooling. This quenching process cooled the samples to room temperature in a time frame ranging from tens of seconds to a few minutes, similar to an air-cooling process. Specific heat treatment protocols included (1) a homogenization heat treatment at 1175 °C for one hour and (2) a homogenization heat treatment at 1175 °C for one hour (the same as (1)) followed by an annealing heat treatment at 720 °C for 16 h.

Samples for X-ray and TEM analyses were prepared following standard metallographic techniques. For high-energy

Fig. 1 Schematic of the bridge structure for AM Bench 2022. This build incorporates four distinct types of legs with dimensions of 0.5 mm, 2.5 mm, 5.0 mm, and a specialized 5.0 mm hollow leg. For the purpose of this study, all specimens were sourced exclusively from the 2.5 mm legs
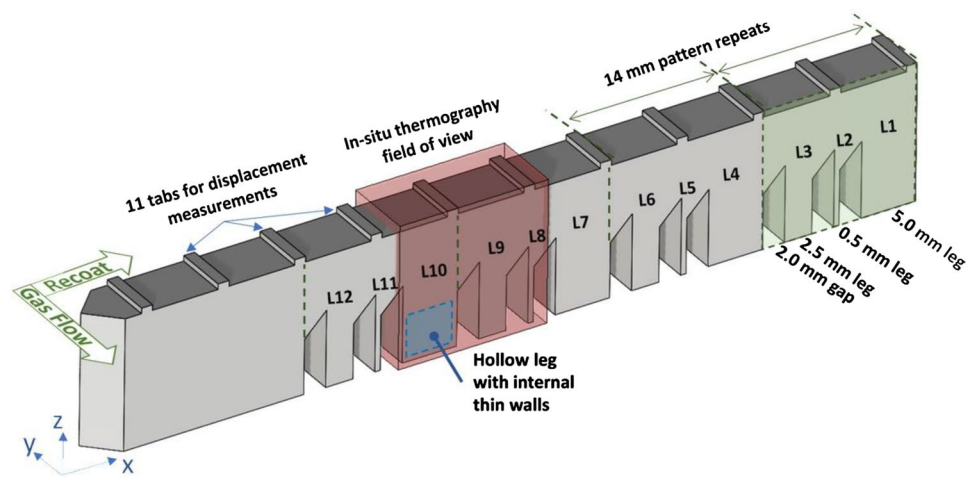
X-ray diffraction measurements, samples were sectioned to approximately 1.2 mm in thickness using a low-speed diamond saw. These were subsequently polished down to about 1 mm thickness on both sides to remove possible near-surface damage layers. In situ X-ray diffraction samples were thinned to roughly 100 μm using 600-grit silicon carbide (SiC) sandpaper, followed by hand polishing with progressively finer grits to achieve a mirror-like surface finish.

For TEM analyses, thin slices of material were initially cut from the bulk sample using a low-speed diamond saw. These slices were then reduced to a thickness of 100 μm using 600-grit SiC paper. 3 mm-diametered disks were extracted from these 100 μm slices using a TEM punch. Electropolishing was employed to decrease the sample thickness further, making them electron-transparent. The electrolyte solution consisted of 60% methanol, 34% butanol, and 6% perchloric acid (comprising 300 ml methanol, 170 ml butanol, and 30 ml perchloric acid). The electropolishing was performed using a Fischione[1] Model 110 twin-jet electropolisher under the following conditions: −10 °C, 30 V, 32 mA, with a jet speed setting 4.

Methods

High-Energy X-Ray Diffraction

High-energy X-ray diffraction (HEXRD) measurements were conducted at the Advanced Photon Source (APS), Argonne National Laboratory, utilizing beamline 11-ID-C. We employed high-energy X-rays with a wavelength of 0.11730 Å, which corresponds to an X-ray energy

of 105.7 keV. The X-ray beam flux density was approximately 1×10^{13} photons/mm²/s, with a beam size of 0.5 mm × 0.5 mm. The sample-to-detector distance was 1250 mm, calibrated using NIST powder diffraction standard reference material (SRM) CeO_2 (SRM 674b).

For the measurements, XRD samples were positioned such that the incident beam was perpendicular to the sample's surface and transmitted through the sample thickness. To capture an average reading over a larger sample volume, the sample was translated in the beam along both vertical and horizontal directions during the measurements. The diffraction patterns were recorded using a two-dimensional area detector. Data reduction and analysis were carried out using GSAS-II software [12].

In Situ X-Ray Scattering

In situ X-ray diffraction measurements were performed at Sector 9 of the APS using the ultra-small-angle X-ray scattering facility [13]. We employed X-rays with a wavelength of 0.5904 Å, equating to an X-ray energy of 21 keV. The measurements combined small-angle X-ray scattering and X-ray diffraction, performed in the transmission geometry on the samples. The beam size used for the diffraction measurements was 0.8 mm × 0.2 mm. Data were collected with a modified Pilatus 300KW detector featuring a pixel size of 172 μm × 172 μm. A single XRD dataset was acquired over an acquisition time of 20 s, and a diffraction pattern was collected approximately every five minutes, giving the in situ measurements, as described below, a time resolution of 5 min. More details about this type of measurement can be found elsewhere [14, 15].

The sample was placed inside a Linkam 1500 heater to facilitate heat treatment. It was sandwiched between two sapphire disks to prevent contact-induced contamination from the furnace. A constant flow of high-purity argon was maintained throughout the measurement to minimize

oxidation. We calibrated the furnace temperature under these operating conditions using NIST SRM 742 (Al_2O_3). The estimated temperature uncertainty was within 5 °C for the temperature range used in this study, and the heating rate was set at 200 °C/min.

The sample-to-detector distance was calibrated using NIST SRM 660a (LaB_6: lanthanum hexaboride) [16]. For data reduction, we used Igor-Pro-based software packages Irena [17] and Nika [18], while detailed XRD data analysis was conducted using a combination of Irena and GSAS-II. In this work, we will focus solely on the X-ray diffraction data.

Transmission Electron Microscopy

TEM and scanning transmission electron microscopy (STEM) data were obtained using a Thermo Fisher Scientific (formerly known as FEI) Titan 80-300. The instrument operated at an accelerating voltage of 300 kV and featured a spherical aberration coefficient of 1.2 mm for TEM measurements. For STEM measurements, the system was equipped with a CEOS CESCOR aberration corrector.

Images in STEM were captured using a probe convergence semi-angle of approximately 14 mrad. High-angle annular dark field (HAADF) and annular dark field (ADF) images were acquired using a Fischione Model 3000 annular detector. The camera length was adjusted such that the inner collection semi-angle was 70 mrad and 23 mrad for HAADF and ADF images, respectively. Incoherent bright field (BF) images were acquired using a circular detector with an outer collection semi-angle of 17 mrad. Additionally, nanobeam electron diffraction (NBED) patterns were collected using a convergence semi-angle of about 1 mrad.

Energy-dispersive spectroscopy (EDS) data were acquired using an EDAX silicon drift detector (SDD). The effective solid angle of the detector was measured using an amorphous Ge film coated on an amorphous SiN support. The maximum effective solid angle, achieved when the holder's penumbra shadowing is minimal, is approximately 0.1 sr.

Four-dimensional STEM (4D-STEM) datasets were collected using a Quantum Detectors Merlin, a direct electron detector based on Medipix3RX technology. These images were captured with a 12-bit depth and an integration time ranging from 2 to 3 ms. The probe convergence semi-angle for these datasets was set to approximately 1 mrad.

For data processing, EDS data were analyzed using the Hyperspy software [19], while 4D-STEM datasets were processed using the LiberTEM software [20]. For the HR-STEM measurements, to minimize image distortions due to sample drift or scan distortions, we used stacked images (typically 16 to 20) acquired with a dwell time of 1 μs. These image stacks were aligned using rigid registration and then summed via the StackReg plugin [21] as implemented in the Fiji software [22].
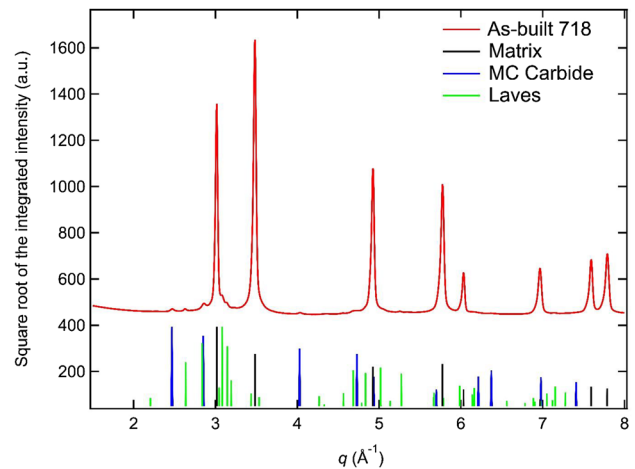

Fig. 2 High-energy X-ray diffraction (HEXRD) pattern of as-built 718. To emphasize weak diffraction peaks, the intensity is displayed as the square root of the integrated intensity. The calculated stick patterns correspond to the matrix phase, MC carbide, and Laves phase. The lattice parameters and symmetries for these phases are detailed in Table 2

Results and Discussion

In this section, we will present our measurement and analysis results, which are divided into three subsections for clarity. The first subsection focuses on characterizing the as-built material through both TEM and XRD, serving as the starting point for understanding the phase transformations. The second subsection delves into the effects of homogenization heat treatment, as monitored by in situ XRD. Lastly, the third subsection examines how the homogenized material responds to extended precipitation heat treatment, utilizing a combination of in situ XRD and ex situ TEM for comprehensive analysis.

As-Built Material

The HEXRD pattern of the as-built material is presented in Fig. 2. This figure displays the intensity as the square root of the integrated intensity, a method used to emphasize weak diffraction peaks from secondary phases. The a-axis is in units of q, where $q = 2\pi/\lambda \sin(\theta)$, is the magnitude of the scattering vector, λ is the X-ray wavelength, and θ being one half of the diffraction angle 2θ.

The diffraction pattern shows that the as-built 718 material primarily consists of a face-centered cubic (FCC) matrix phase with a lattice parameter of (3.608 ± 0.001) Å. In addition to the dominant FCC phase, two secondary phases are present: a hexagonal Laves phase with lattice parameters of $a = (4.781 \pm 0.003)$ Å and $c = (7.875 \pm 0.002)$ Å, and an FCC MC carbide phase with a lattice parameter of (4.410 ± 0.003) Å. The uncertainties for the XRD are of

Table 3 Phases identified in the as-built 718 by high-energy X-ray diffraction and TEM

Phase	Symmetry	HEXRD lattice parameter a (Å)	HEXRD lattice parameter c (Å)	TEM lattice parameter a (Å)	TEM lattice parameter c (Å)
matrix	Fm-3m	3.608 ± 0.001		*	
MC carbide	Fm-3m	4.410 ± 0.003		4.42 ± 0.02	
Laves	P63/mmc	4.781 ± 0.003	7.875 ± 0.002	4.78[#]	8.32[#]

*The matrix lattice parameter of 3.608 Å based on HEXRD measurements was assumed to calibrate lattice parameter analysis of the MC and Laves phases

[#]No uncertainty is included because this value is based on the measurement of one particle and therefore no standard deviation about the mean exists
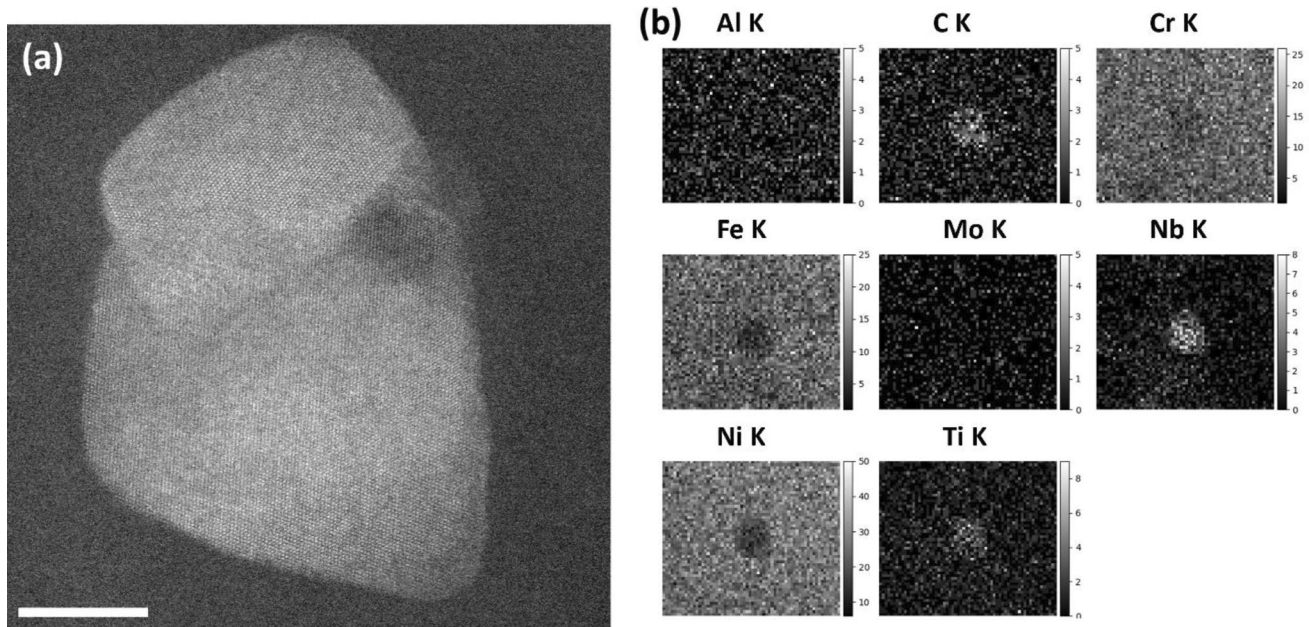
Fig. 3 a HAADF-STEM image and corresponding **b** EDS elemental maps of two MC carbides in the as-built 718. The carbides are enriched in Nb, Ti, and C. The scale bar is equal to 10 nm for **a**

Type B and represent one standard deviation from the mean. These lattice parameters, together with the lattice parameters estimated using TEM, are reported in Table 3.

MC carbides are commonly found in nickel-based super-alloys [23, 24], so their presence in AM nickel-based materials such as 718 is unsurprising [14, 25]. While the formation of MC carbide in conventionally manufactured 718 is often associated with aging heat treatment [23], these carbides are also known to form during AM processes. This is due to the numerous nucleation sites created by the complex thermal cycles that occur during AM processing of the carbides. Additionally, the heterogeneous elemental distribution resulting from AM conditions creates a favorable environment for MC carbide formation. Once formed, MC carbides are thermally stable owing to their high melting point, making it likely for them to persist in the material's microstructure.

The formation of the Laves phase in AM nickel-based superalloys has also been previously reported in the AM literature [26, 27]. In AM, localized variations in chemical composition can occur, making areas such as the interdendritic regions or grain boundaries susceptible to the nucleation and growth of the Laves phase [27]. The presence of this phase is generally considered detrimental to mechanical properties, as it can act as a point of crack initiation and reduce the material's ductility and toughness.

The microscopic TEM data are consistent with the bulk X-ray results. Figure 3 presents the HAADF-STEM image of two MC carbides overlapping in projection, exhibiting a combined ellipsoidal shape and enriched in Nb, Ti, and C. These carbides possess an FCC lattice that is incoherent with the matrix. Utilizing NBED for measurement, and an internal calibration based on an assumed lattice parameter of 3.608 Å for the matrix, the lattice parameter of the MC
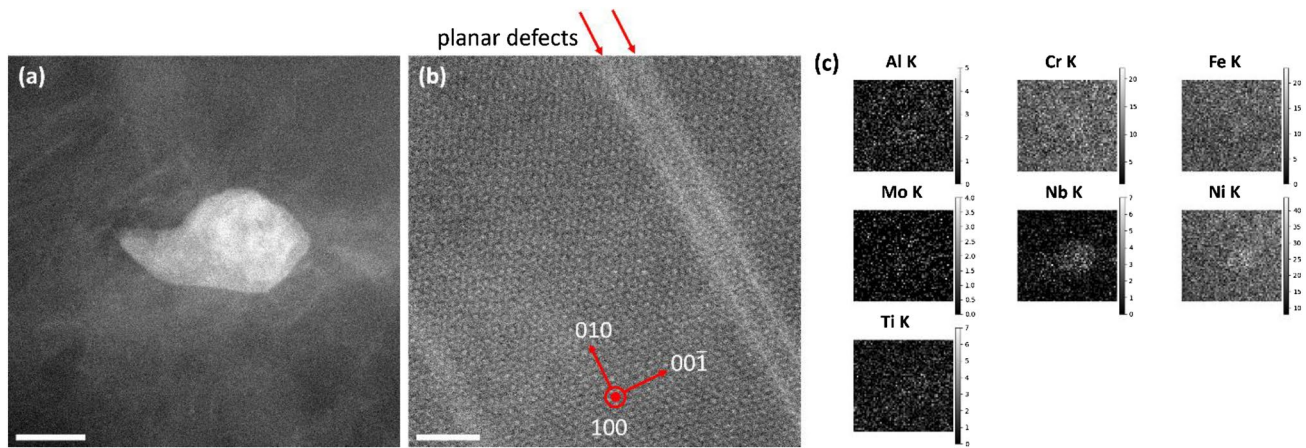
Fig. 4 **a** ADF-STEM image of a C14 Laves precipitate in the as-built 718. **b** An atomic resolution TEM image of a Laves precipitate showing the presence of planar defects. **c** EDS elemental maps show the precipitate is enriched in Nb. The scale bars are equal to 50 nm for **a** and 2 nm for **b**, respectively

carbide is estimated to be (4.42 ± 0.02) Å based on the measurement of two particles. To estimate the size of the MC carbide, we employed a circular approximation method for ellipsoids. The process involved manual ellipse fitting, where an ellipse was aligned with the contour of the carbide. We calculated the diameter of a circle that has the same area as the ellipse we fitted. This diameter gave us an approximate measurement of the object's size. A set of five measurements yielded an average MC carbide size of 35.1 nm with a standard deviation of 8.9 nm. The uncertainty reported for all TEM measurements here and below represents one standard deviation around the mean.

Figure 4 presents STEM data on the Laves phase. Utilizing high-resolution STEM imaging shown in Fig. 4a, we estimated the diameter of a single identifiable C14 Laves phase precipitate to be approximately 107.1 nm, employing the same ellipse-fitting method as used for the MC carbides. Additionally, Fast Fourier Transform (FFT) analysis was carried out on this high-resolution image. The FFT reflections, sourced from two separate images and using previously calibrated scale information, enabled us to estimate the lattice parameters for the Laves phase: $a = 4.78$ Å and $c = 8.32$ Å. It should be noted that these estimates are subject to limitations in accuracy due to the constraints of the STEM's embedded scale information and image distortions due to sample drift. Moreover, we observed the presence of planar defects within the Laves phase (Fig. 4b), a phenomenon also reported in previous studies [28–30]. Interestingly, these defects are believed not to arise from the slip mechanism on the (001) basal plane, which is the most common deformation process in hexagonal polytypes because the basal plane in an HCP structure has the highest planar density. Moreover, similar planar defects were observed to persist even after prolonged high-temperature annealing,

suggesting their inherent stability [28]. The formation of such planar defects could be attributed to localized high-stress conditions induced by the AM process. Further investigation is needed to fully understand its nature. Elemental analysis indicates an enrichment in Nb relative to the matrix, as shown in Fig. 4c. The analysis also indicated a slight increase in Mo and Ti along with a slight decrease in Ni, Fe, and Cr, although these changes were not statistically significant.

The TEM data for the γ matrix in the as-built 718 are detailed in Figs. 5 and 6. The HAADF and BF images in Fig. 5 reveal a columnar, cellular structure. The HAADF image shows signs of elemental microsegregation in intercellular regions, the increase in intensity suggests higher atomic number elements like Nb. This behavior has been observed elsewhere [29, 31] and aligns with the phenomenon of solute rejection that occurs during rapid solidification induced by the fast cooling rates and high thermal gradients inherent to AM. Such solute microsegregation has been widely observed in AM-produced nickel-based superalloys [4, 32] and often leads to the formation of unexpected phases like the δ phase [33, 34] and Laves phase [27], as we have also observed in this study.

The higher-magnification BF image in Fig. 5c displays contrasts indicative of dislocations and precipitates. A high dislocation density in as-built AM materials is expected due to rapid cooling rates, steep thermal gradients, and the layer-by-layer building process, all of which can introduce mechanical stresses and non-equilibrium microstructures. The typical spacing between intercellular regions in the image is about 0.3 μm. This value is consistent with previously observed dendritic arm spacings in AM-produced nickel alloy 625 [27], fabricated under similar processing conditions.
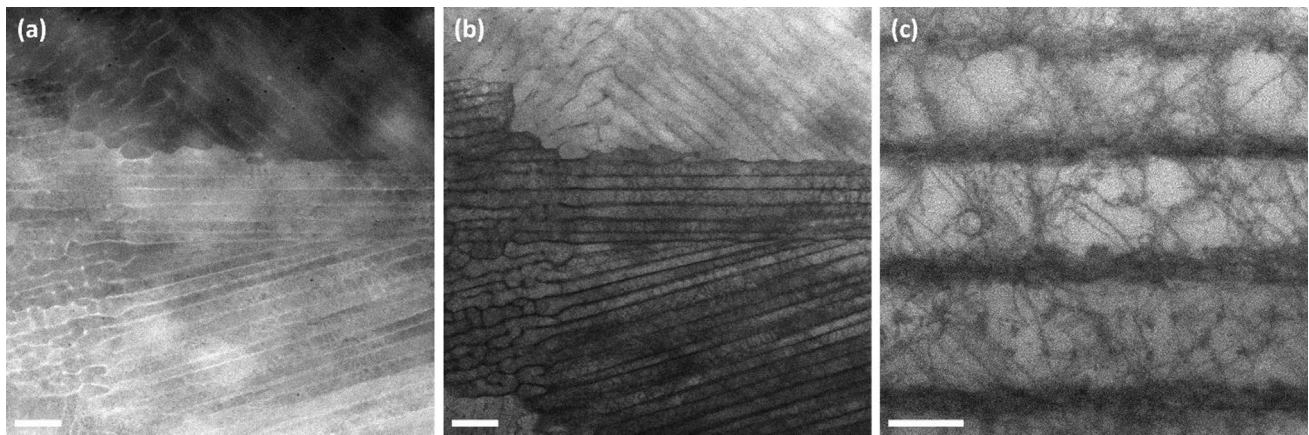
Fig. 5 **a** HAADF and **b** BF images of the as-built 718. **c** Higher-magnification BF image showing the presence of dislocations and precipitates. The scale bars are equal to 1 μm for **a** and **b**, and 0.2 μm for **c**
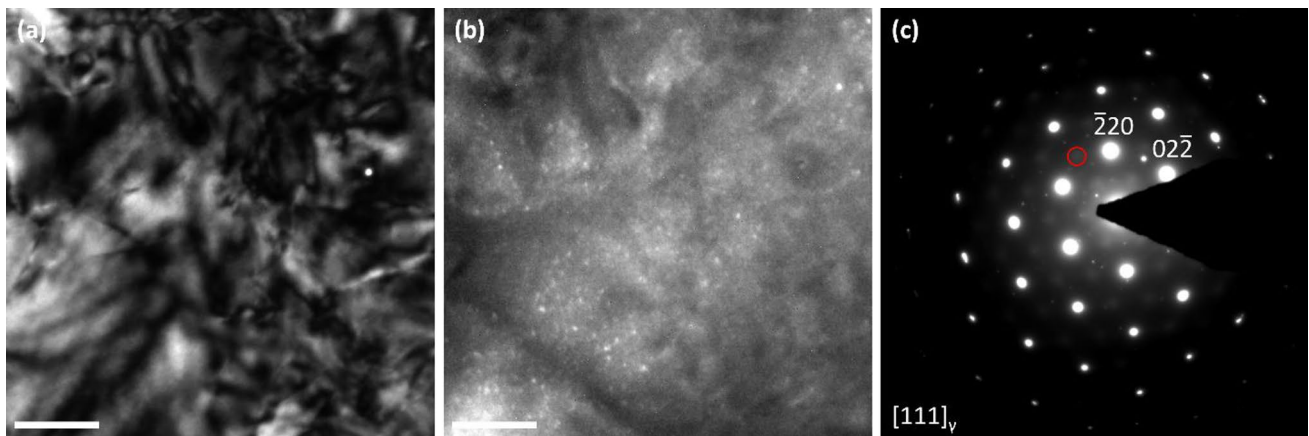

Fig. 6 **a** Bright field and **b** dark field TEM observations of the as-built 718 viewed along <111>$_\gamma$. The intensity of the **c** SAED pattern has been scaled to increase visibility of weak reflections. For the dark field image shown in **b**, the objective aperture was selected in accord-ance with the red circle in the SAED pattern, to highlight the formation of the unidentified nanoscopic precipitates. The scale bars are equal to 50 nm for **a** and **b**

For completeness, we also note that unidentified nanoscale precipitates also exist in the as-built 718. Figure 6 provides TEM observations of the as-built 718 material, viewed along the <111>$_\gamma$ direction. Panel (a) shows BF imaging, while panel (b) presents dark-field (DF) imaging. The selected area electron diffraction (SAED) pattern's intensity has been scaled to enhance the visibility of weaker reflections. Alongside the sharp reflections characteristic of the γ matrix, we also observed broad reflections in the diffraction pattern. These broad reflections are attributed to the presence of nanoscale precipitates, which are approximately 1 nm to 3 nm in diameter. These precipitates were identified using DF imaging, using the reflection highlighted by the red circle in the SAED patterns as the objective aperture. The small size of these precipitates accounts for the broad nature of the reflections in the SAED pattern and the lack

of detection in the XRD measurements. While the phase associated with these precipitates has not yet been indexed, it is highly unlikely to be among the common phases in 718, such as γ, γ', γ", MC, Laves, and δ. Additional sharp reflections not associated with the gamma matrix are present in the SAED pattern. The d-spacing of these reflections were consistent with the Laves phase.

Homogenization Heat Treatment

Homogenization heat treatment is often required for AM nickel-based superalloys for several key reasons [35]. First, the treatment aims to achieve microstructural homogeneity by reducing or eliminating the significant heterogeneities induced by AM processes, such as microsegregation and anisotropic grain structures. Second, it helps dissolve unwanted
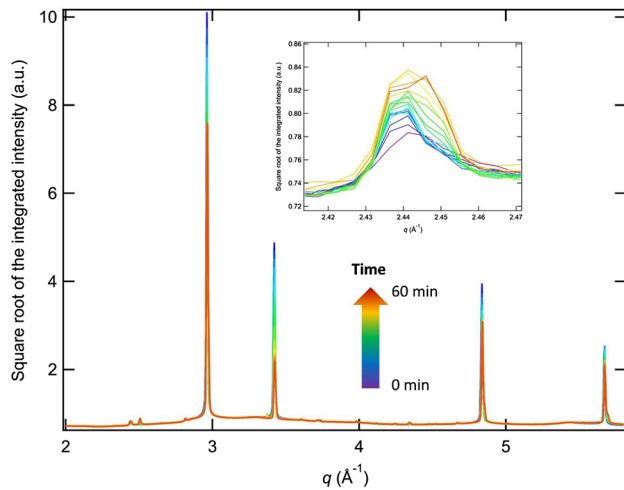
Fig. 7 The in situ XRD data acquired during a homogenization heat treatment conducted at 1175 °C for 1 h. The XRD data were acquired approximately every 5 min, and their acquisition time is denoted by their respective color, as illustrated by the color arrow. The inset shows the evolution of the MC {111} peak and follows the same color scheme as in the color arrow

Fig. 8 Evolution of the carbide volume fraction as a function of time during the homogenization heat treatment

phases that may have formed during the AM process. Third, the treatment can also relieve the often-high levels of localized residual stress generated by the AM techniques. Collectively, these benefits lead to an improved and thermally stable microstructure, aligning well with the alloy's intended high-temperature applications.

For this study, we incorporated a one-hour homogenization treatment at 1175 °C into our heat treatment procedure, which is just below the material's incipient melting temperature. To investigate structural variations during this homogenization process, we carried out in situ XRD measurements. The corresponding data are displayed in Fig. 7, where we have plotted the square root of the diffraction intensity to emphasize the peaks associated with secondary phases.

Several key observations emerge from the in situ data acquired during the homogenization heat treatment. Most importantly, the diffraction peaks corresponding to the Laves phase are absent in the in situ data, starting from the first XRD dataset acquired at 1175 °C. Given a heating rate of 200 °C/min, this indicates rapid dissolution of the Laves phase during the heating process and the few (< 5) minutes prior to the first XRD measurement. The thermal stability of this phase is strongly influenced by the localized concentration of Nb. Elevated temperatures increase Nb mobility, promoting a more uniform elemental distribution and pushing the Nb concentration toward approximately 5.5% by mass, the mass fraction present in the original feedstock powder. As a result, the Laves phase becomes thermodynamically unstable at temperatures above approximately 1050 °C, leading to its dissolution. The accelerated dissolution of the
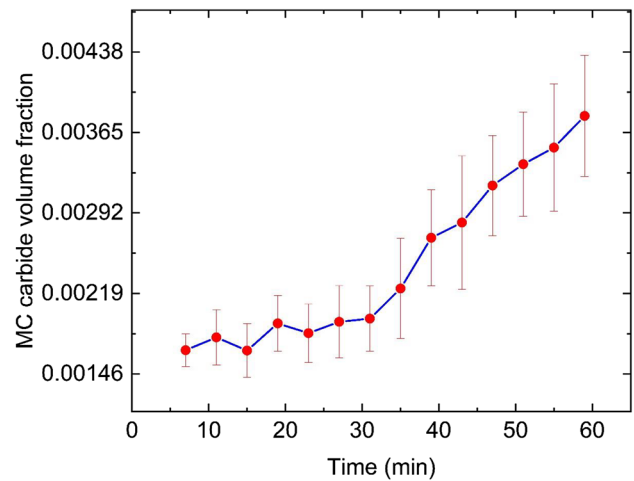
Laves phase observed in our study during homogenization heat treatment may be influenced by the proximity of the selected homogenization temperature to the incipient melting point, where atomic mobility is high. This is in contrast to previous work, which also noted dissolution behavior during homogenization, albeit at a slower rate [36].

Conversely, the MC carbides remained present throughout the homogenization heat treatment, suggesting its thermal stability. Their peak widths, as demonstrated by the inset (MC {111} peak) decreased, suggesting the coarsening of these carbides and consistent with previous work investigating the response of the 718 microstructures to the homogenization heat treatment [37]. This coarsening is likely facilitated by Ostwald ripening to minimize the total interfacial energy. However, such coarsening may adversely affect mechanical properties, such as hardness and wear resistance.

The total volume fraction of MC carbides also increased during the homogenization heat treatment, as shown in Fig. 8. The volume fraction analysis was conducted following a method described in detail elsewhere [34]. These MC carbides are typically rich in Nb. This increase in volume may be linked to the dissolution of the Laves phase, which is also rich in Nb in 718 [38]. The dissolution of the Laves phase could provide the necessary Nb source for the nucleation and growth of MC carbides, thereby contributing to the overall increase in their volume fraction. This in situ data, obtained from a constant-volume setup, can be used for comparison and validation against both experimental observations and kinetic models [39].

The diffraction peaks corresponding to the FCC matrix also narrowed, indicating grain growth and/or a reduction in lattice defects. Both of these changes are typical results of homogenization heat treatment [4, 14]. Additionally, a change in texture was observed, as evidenced by the altered

ratio of relative peak intensities. For instance, the intensity ratio of the {111} to {200} peaks started at ≈ 4 but increased to ≈ 11 by the end of the heat treatment, suggesting preferred grain growth along the $<111>$ direction and development of a specific texture. It should be noted that this heat treatment was conducted on a foil approximately 100 μm thick, which could impose constraints on texture development.

Overall, these results, namely the dissolution of the Laves phase, coarsening of the MC carbides, and peak narrowing and texture development in the FCC matrix, emphasize the need for careful optimization of both the duration and temperature of homogenization heat treatments to achieve the desired microstructural properties.

Finally, we observed that the heat treatment led to the formation of an unidentified secondary phase or multiple phases with complex structures, likely oxides. Despite the use of high-purity argon, heat treatment at elevated temperatures in the in situ furnace inevitably resulted in oxide formation on the surface of the homogenized material. XRD measurements are particularly sensitive to such oxide formations when conducted on thin foil specimens due to their larger specific surface area. However, this oxide formation is generally not a significant concern for standard homogenization heat treatments of bulk materials, including the in-house homogenization process we carried out in preparation for the aging experiments.

Homogenized and Aged Material

718 is engineered to be a precipitation-hardenable alloy. The formation of finely dispersed γ' and γ'' precipitates impedes dislocation movement, which is crucial for achieving the alloy's desired properties, including strength, creep resistance, fatigue resistance, and thermal stability. Accurate microstructure modeling is key to fine-tuning these characteristics by controlling the precipitates' size, distribution, and volume fraction, thereby optimizing the material for specific applications. To validate such models, we conducted both in situ and ex situ measurements using synchrotron X-rays and TEM. These data serve as a benchmark to validate the predictive models for the critical heat treatment steps essential to AM 718's performance.

In the ex situ study, we conducted measurements on samples that underwent homogenization at 1175 °C, followed by aging heat treatment at 720 °C for 16 h; both procedures were carried out in argon back-filled evacuated ampules. HEXRD results are presented in Fig. 9. XRD analysis revealed three distinct phases: the matrix, γ'', and MC carbide. We also suspect the presence of γ', a primary strengthening phase in 718, within the matrix. However, its identification is challenging through XRD analysis, as γ' is coherent with the matrix and possesses a nearly identical lattice parameter, typically exhibiting a misfit of less than
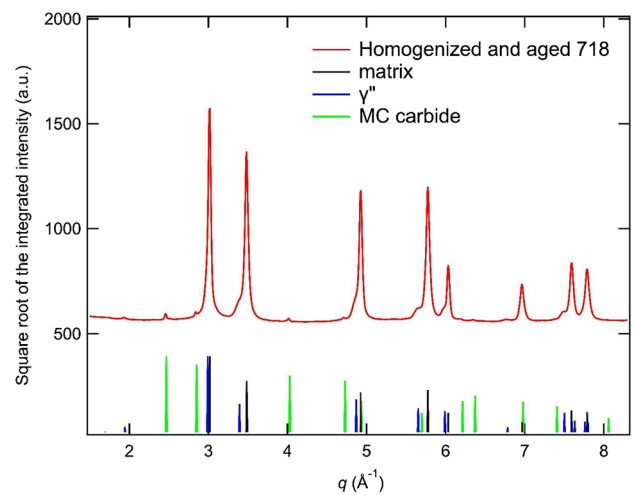

Fig. 9 HEXRD pattern of AM 718 after a homogenization heat treatment at 1175 °C for 1 h followed by an aging heat treatment at 720 °C for 16 h. To emphasize weak diffraction peaks, the intensity is displayed as the square root of the integrated intensity. The calculated stick patterns correspond to the matrix phase, MC carbide, and γ'' phase. The lattice parameters and symmetries for these phases are detailed in Table 3

2% for nickel-based superalloys [40]. For this reason, we calculated the lattice parameters for the matrix phase, MC carbide, and the γ'' phase, and these are summarized in Table 4.

TEM offers a more detailed microscopic perspective on the formation of these precipitates in the aged material. We observed the expected types of precipitation, including γ'' and MC carbide, which were identified by HEXRD, as well as the γ' precipitates that cannot be resolved using HEXRD. TEM also uniquely enables us to gain insights into precipitation behavior and orientation relationships. Some of these TEM results are provided as follows:

We observed a high concentration of well-dispersed, nanoscopic γ'' precipitates in the homogenized and aged 718 alloy (Fig. 10). These precipitates exhibited the expected lenticular morphology elongating normal to the c axis of the tetragonal unit cell [41] and maintained a specific orientation relationship with the γ matrix, described as $\{001\}_{\gamma''}//\{001\}_{\gamma}$ and $[100]_{\gamma''}//[100]_{\gamma}$. Three orientation variants were identified, where the c-axis of the γ'' precipitates aligned with the [100], [010], or [001] directions of the γ matrix.

Dimensional analysis, based on 131 measurements using virtual dark-field images reconstructed from 4D-STEM data, indicated that the long and short dimensions of the γ'' precipitates are measured at (19.8 ± 8.3) nm and (6.9 ± 2.3) nm, respectively. These images were generated by summing the $\{002\}_{\gamma''}$, $\{011\}_{\gamma''}$, and $\{013\}_{\gamma''}$ reflections. These measurements did not distinguish if the γ'' was isolated or in the form of a coprecipitate (vide infra).

High-resolution STEM (HR-STEM) measurements revealed a small lattice parameter misfit. Here, the lattice

Table 4 Phases identified in the aged 718 by high-energy X-ray diffraction

Phase	Symmetry	HEXRD lattice parameter a (Å)	HEXRD lattice parameter c (Å)	TEM lattice parameter a (Å)	TEM lattice parameter c (Å)
matrix	Fm-3m	3.608 ± 0.001		*	
MC carbide	Fm-3m	4.424 ± 0.002		4.42 ± 0.02	
γ''	I4/mmm	3.602 ± 0.003	7.409 ± 0.005	3.61 ± 0.10	7.41 ± 0.28

*The matrix lattice parameter of 3.608 Å based on HEXRD measurements was assumed to calibrate lattice parameter analysis of the MC and γ'' phases
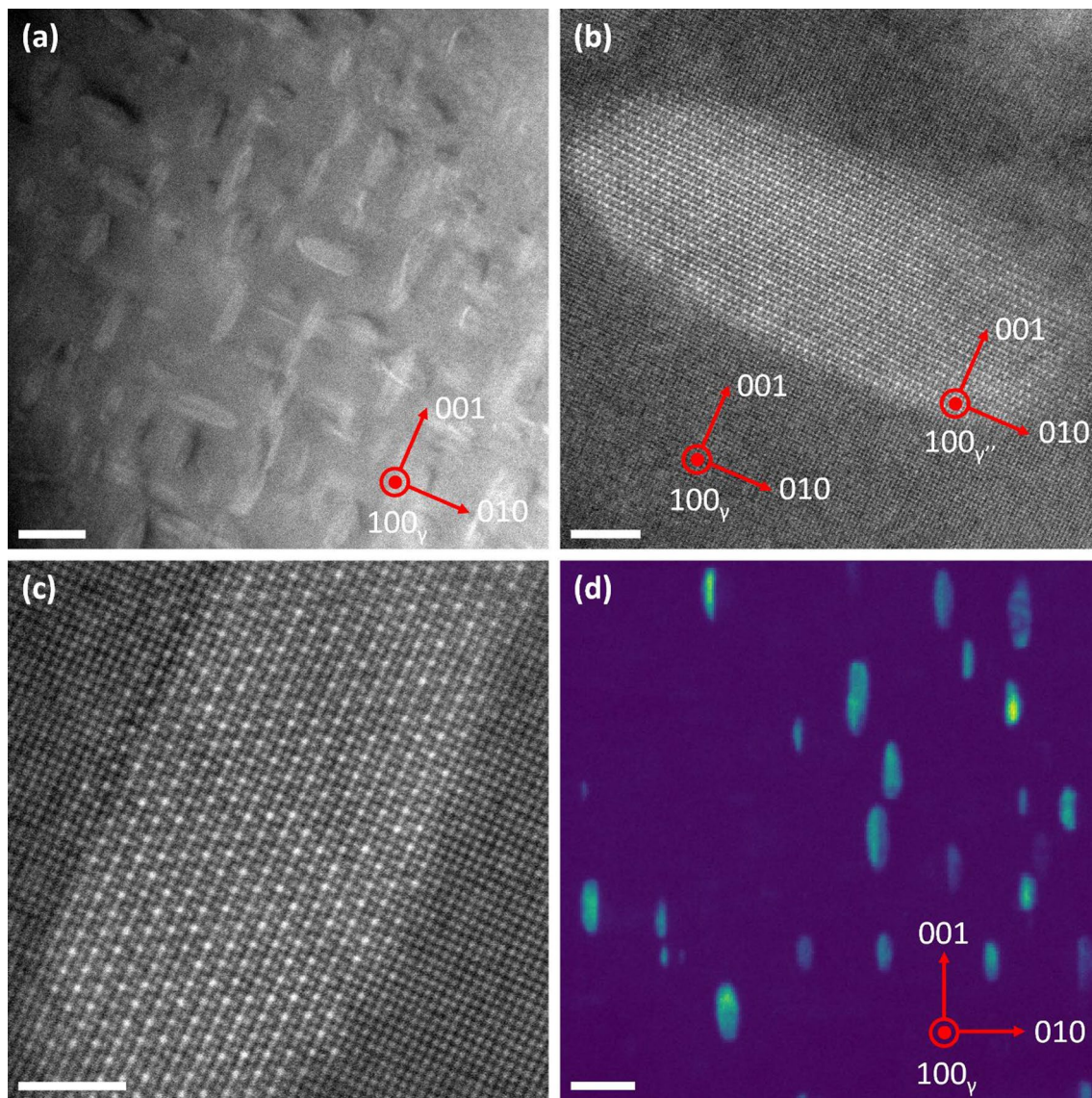
Fig. 10 a STEM observation of the γ'' precipitates in the aged AM 718 and **b** Orientation relationship between γ and γ''. **c** Chemical ordering within the precipitate is evident. **d** A virtual dark field image generated by integrating over Bragg reflections specific to one γ'' orientation variant. Scale bars are equal to 25 nm for **a** and **d**, 3 nm for **b**, and 2 nm for **c**

spacings were computed, using the γ matrix as an internal reference (assumed to be 3.608 Å), by manual analysis of the FFT. Based on 9 precipitates, the c-parameter of the γ'' phase was found to be (7.41 ± 0.28) Å, while the a-parameter was (3.61 ± 0.10) Å. This level of misfit is consistent with previous observations [42], and the high coherence strain induced
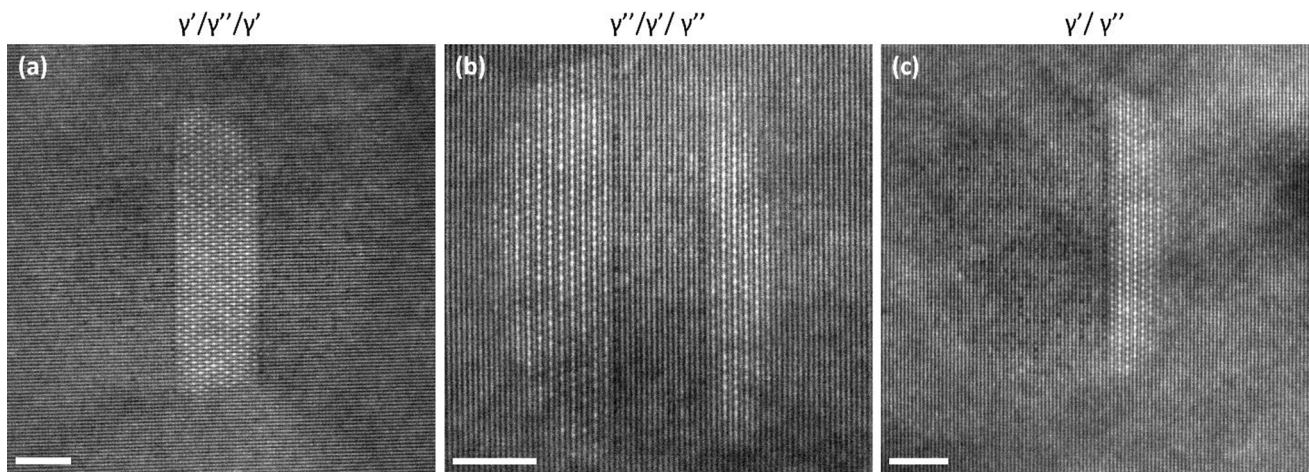
$\gamma'/\gamma''/\gamma'$ $\gamma''/\gamma'/\gamma''$ γ'/γ''

Fig. 11 γ' phase in HT718 viewed along $<100>_\gamma$. In the cases where γ' precipitates were observed, they form in conjunction with γ''. The interface between γ' and γ'' is coherent. Three different configurations are shown above **a** $\gamma'/\gamma''/\gamma'$, **b** $\gamma''/\gamma'/\gamma''$, and **c** γ'/γ''. The scale bars are equal to 3 nm

by the lattice misfit contributes to the overall strength of the material. Notably, no dislocations were observed in the high-resolution images when viewed along the $<100>_\gamma$ or $<110>_\gamma$ directions, indicating that the γ'' precipitates are coherent with the γ matrix.

Figure 11 presents atomic-resolution images of γ' precipitates in aged 718, with all images taken along the $<100>_\gamma$ viewing direction. Due to the structural similarity between γ' and the γ matrix, identifying γ' is challenging, similar to XRD. However, when γ' was successfully observed, three distinct coprecipitate configurations were noted: a "sandwich" structure with a $\gamma'/\gamma''/\gamma'$ arrangement as shown in Fig. 11a, another "sandwich" structure but with a $\gamma''/\gamma'/\gamma''$ arrangement as shown in Fig. 11b, and a neighboring structure involving γ' and γ'' as shown in Fig. 11c. In these observed configurations, γ' and γ'' share a coherent interface. Because the atomically flat γ'–γ'' interface departs from the lenticular shape of the γ'' precipitates it can be used to infer the presence of γ'–γ'' coprecipitates, while FFT analysis of atomic resolution images can subsequently confirm the presence of γ'. Typically, γ' and γ'' precipitate independently during heat treatment of 718 [43]. However, previous studies have suggested that by adjusting the alloy's composition, the precipitation of γ'' can be delayed, leading to the coprecipitation of γ'' and γ', with γ'' nucleating on pre-existing γ' [44, 45]. While the precipitation behaviors in (b) and (c) align phenomenologically with this hypothesis, the sandwich structure in (a), where γ'' is flanked by two γ' precipitates, suggests the presence of a solute depletion zone. In this zone, the formation of γ' could create a chemical composition favorable for γ'' nucleation, particularly at interfaces with lower interfacial energy compared to the situation for homogeneous nucleation of γ'' from the matrix.

Coprecipitation is an active field of research [46]. Additional evidence from this alloy system, such as ex situ characterization of precipitate formation in samples aged for shorter time periods or in situ observations, will enhance our understanding of the coprecipitation mechanisms.

The morphologies of the γ' and γ'' precipitates in such a coprecipitation scenario are also worth noting. While γ'' precipitates are typically disk-shaped and γ' precipitates are usually cuboidal [41], Fig. 11 reveals that both types of precipitates in this case are disk-like, each with major and minor dimensions. For γ' coprecipitates, based on nine measurements, the dimensions were found to be (14.8 ± 3.4) nm and (6.1 ± 2.0) nm, respectively. For this dimensional analysis, we employed FFT filtering focused on reflections unique to the γ' phase to improve contrast between γ and γ'. While the dimensions of γ'' coprecipitates, based on ten measurements, were (15.3 ± 4.8) nm and (3.9 ± 1.6) nm, respectively. Additionally, it is worth noting that the TEM data are not sufficient to discern the lattice parameter misfit between γ' and γ. Limited EDS data indicated the presence of Nb, Ti, Al, and Ni in γ'.

Within the homogenized and aged 718, we also observed MC carbides. The associated TEM images are shown in Fig. 12. The MC carbide is incoherent with the matrix and has undergone significant coarsening compared to its initial structure. Using the same ellipse-fitting method as in previous analyses, an average particle diameter of (399 ± 221) nm was determined based on 24 measurements. For accuracy, particles located at the edge of the foil, such as the one shown in Fig. 12(b), were excluded from this analysis. The lattice parameter for MC carbide was estimated to be (4.42 ± 0.02) Å, a value derived from three separate measurements. These measurements were conducted using NBED
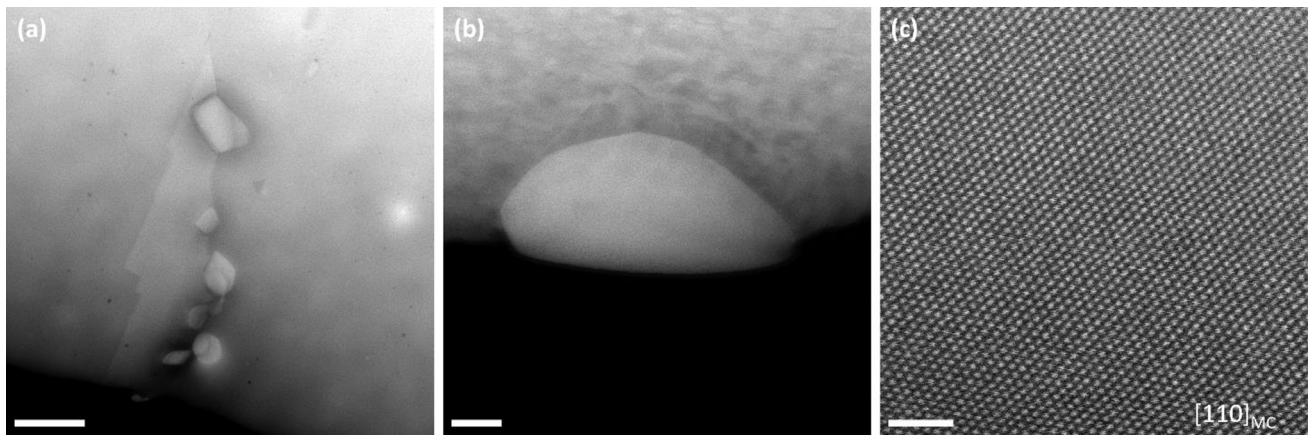
Fig. 12 **a**, **b** HAADF images showcasing coarsened MC carbides following aging heat treatment on a homogenized sample; **c** Atomic-resolution image of an MC carbide. Scale bars are equal to 1.5 μm for **a**, 50 nm for **b**, and 2 nm for **c**, respectively
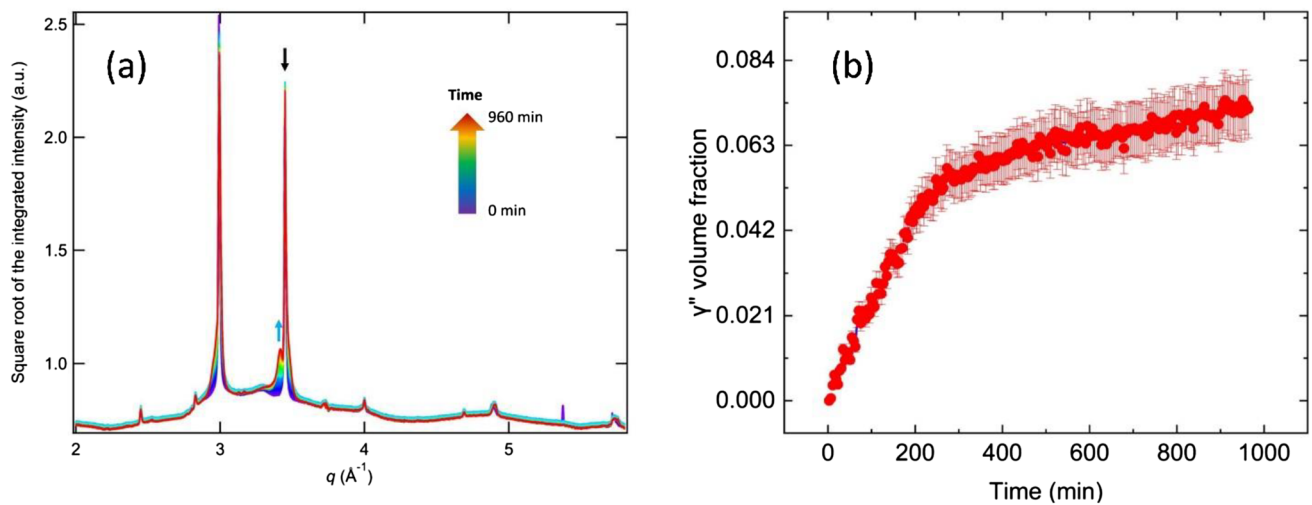

Fig. 13 **a** In situ X-ray data displaying a monotonic decrease in the γ intensity (indicated by a black arrow) while concurrently showing a monotonic increase in the γ" intensity (indicated by a green arrow). **b** Time-dependent evolution of the volume fraction of the γ" precipitates

patterns and were internally calibrated with the matrix lattice parameter assumed to be 3.608 Å. It is also worth noting that some MC carbides were found to contain pores, although the mechanism behind their formation remains unclear.

Finally, to investigate phase transformation kinetics during the aging process, we conducted in situ XRD measurements at 720 °C for 16 h. The full dataset is displayed in Fig. 13a, with the time of acquisition indicated by a color scale. The data reveal a consistent decrease in matrix diffraction intensity, represented by the downward black arrow marking the γ {200} peak. In contrast, we saw a steady increase in a set of peaks absent in the as-homogenized material, corresponding to the γ" phase. This is highlighted by the upward-pointing green arrow, which marks the γ" {220} peak. The time-dependent volume fraction of γ" is also presented in Fig. 13b, showing a rapid increase during the first four hours of heat treatment, followed by a slower, yet continuous, increase. On the other hand, the XRD signatures associated with MC carbide, such as peak position and integrated intensity, remained unchanged throughout the aging process. This suggests that the carbide is stable, and any observed coarsening in the TEM images likely resulted from the earlier homogenization heat treatment.

Conclusions

The microstructural development in AM materials is critical for their performance, qualification, and certification. Due to the complex nature of AM processes, rigorous

benchmark data are essential for validating ongoing improvements in microstructural models. In this study, aligned with the 2022 AM-Bench Challenge CHAL-AMB2022-01-PE, we characterized the phase composition and phase evolution in AM 718. We examined the material in its as-built state and its response to homogenization and subsequent aging heat treatments. Our main findings include:

1. In the as-built 718, we identified two secondary phases: an MC carbide and a C14 Laves phase. The MC carbides are ellipsoidal in shape and have an equivalent diameter of $(35.1 \pm 8.9$ nm). We observed planar defects in the Laves phase for the single example that was measured. We also observed the presence of well-dispersed, unidentified nanoscopic precipitates that are 1 nm to 3 nm in size throughout the matrix.

2. During homogenization heat treatment at 1175 °C, the Laves phase dissolves rapidly (in less than five minutes). MC carbides remain stable but experience coarsening. An increase in the total volume of MC carbides occurs, likely facilitated by the dissolution of the Nb-rich Laves phase. During the treatment, the γ matrix develops a pronounced texture. The narrowing of the XRD peak suggests either an increase in grain size or a decrease in defects within the matrix.

3. The aging heat treatment applied to the homogenized AM 718 resulted in the formation of strengthening γ' and γ" phases. MC carbide remained stable throughout the aging process. Bulk high-energy X-ray diffraction data determined the lattice parameters for the matrix, γ", and MC carbide following the heat treatment. Both XRD and TEM from this study lacked the sensitivity to discern the lattice parameters of the coherent γ' phase.

4. TEM measurements reveal that the well-dispersed γ" precipitates exhibit the expected disk-like morphology, with long and short dimensions measuring (19.8 ± 8.3) nm and (6.9 ± 2.3) nm, respectively. These γ" precipitates maintain a specific orientation relationship with the matrix, conforming to $\{001\}_{\gamma''}//\{001\}_{\gamma}$ and $[100]_{\gamma''}//[100]_{\gamma}$. On the other hand, the observed γ' displays complex coprecipitation behavior with γ" and surprisingly also takes on a disk-like shape, deviating from its expected cuboidal morphology. In situ XRD unambiguously captures the transformation from the matrix to γ" and tracks the growth kinetics of γ" throughout the aging heat treatment.

References

1. Wei H, Mukherjee T, Zhang W, Zuback J, Knapp G, De A, DebRoy T (2021) Mechanistic models for additive manufacturing of metallic components. Prog Mater Sci 116:100703
2. Levine L, Lane B, Heigel J, Migler K, Stoudt M, Phan T, Ricker R, Strantza M, Hill M, Zhang F (2020) Outcomes and conclusions from the 2018 AM-bench measurements, challenge problems, modeling submissions, and conference. Integr Mater Manuf Innov 9:1–15
3. Levine L, Lane B, Becker C, Belak J, Carson R, Deisenroth D, Glaessgen E, Gnaupel-Herold T, Gorelik M, Greene G, Habib S, Higgins C, Hill M, Hrabe N, Kilgore J, Kim JW, Lemson G, Migler K, Rowenhorst D, Moylan S, Pagan D, Phan T, Praniewicz M, Stoudt M, Schwalbach E, Seppala J, Weaver J, Yeung H, Zhang F (2023) Outcomes and conclusions from the 2022 AM bench measurements, challenge problems, modeling submissions, and conference. Integr Mater Manuf
4. Zhang F, Levine LE, Allen AJ, Campbell CE, Lass EA, Cheruvathur S, Stoudt MR, Williams ME, Idell Y (2017) Homogenization kinetics of a nickel-based superalloy produced by powder bed fusion laser sintering. Scripta Mater 131:98–102
5. Liu Z, Zhao D, Wang P, Yan M, Yang C, Chen Z, Lu J, Lu Z (2022) Additive manufacturing of metals: microstructure evolution and multistage control. J Mater Sci Technol 100:224–236
6. Idell Y, Levine LE, Allen AJ, Zhang F, Campbell CE, Olson G, Gong J, Snyder D, Deutchman H (2016) Unexpected δ-phase formation in additive-manufactured Ni-based superalloy. JOM 68:950–959
7. Guo Q, Qu M, Chuang CA, Xiong L, Nabaa A, Young ZA, Ren Y, Kenesei P, Zhang F, Chen L (2022) Phase transformation dynamics guided alloy development for additive manufacturing. Addit Manuf 59:103068

8. Mukherjee T, Elmer J, Wei H, Lienert T, Zhang W, Kou S, DebRoy T (2023) Control of grain structure, phases, and defects in additive manufacturing of high-performance metallic components. Prog Mater Sci 101153

9. Zhang F, Levine LE, Allen AJ, Young SW, Williams ME, Stoudt MR, Moon K-W, Heigel JC, Ilavsky J (2019) Phase fraction and evolution of additively manufactured (AM) 15–5 stainless steel and inconel 625 AM-bench artifacts. Integr Mater Manuf Innov 8:362–377

10. Lane B, Mekhontsev S, Grantham S, Vlasea M, Whiting J, Yeung H, Fox J, Zarobila C, Neira J, McGlauflin M (2016) Design, developments, and results from the NIST additive manufacturing metrology testbed (AMMT). In: 2016 International solid freeform fabrication symposium, University of Texas at Austin

11. Amb2022-01 benchmark measurements and challenge problems. https://www.nist.gov/ambench/amb2022-01-benchmark-measurements-and-challenge-problems (2023)

12. Toby BH, Von Dreele RB (2013) Gsas-II: the genesis of a modern open-source all purpose crystallography software package. J Appl Crystallogr 46(2):544–549

13. Ilavsky J, Zhang F, Andrews RN, Kuzmenko I, Jemian PR, Levine LE, Allen AJ (2018) Development of combined microstructure and structure characterization facility for in situ and operando studies at the advanced photon source. J Appl Crystallogr 51(3):867–882

14. Zhang F, Levine LE, Allen AJ, Stoudt MR, Lindwall G, Lass EA, Williams ME, Idell Y, Campbell CE (2018) Effect of heat treatment on the microstructural evolution of a nickel-based superalloy additive-manufactured by laser powder bed fusion. Acta Mater 152:200–214

15. Jia Q, Zhang F, Rometsch P, Li J, Mata J, Weyland M, Bourgeois L, Sui M, Wu X (2020) Precipitation kinetics, microstructure evolution and mechanical behavior of a developed Al–Mn–Sc alloy fabricated by selective laser melting. Acta Mater 193:239–251

16. Black DR, Windover D, Henins A, Filliben J, Cline JP (2011) Certification of standard reference material 660b. Powder Diffr 26(2):155–158

17. Ilavsky J, Jemian PR (2009) Irena: tool suite for modeling and analysis of small-angle scattering. J Appl Crystallogr 42(2):347–353

18. Ilavsky J (2012) Nika: software for two-dimensional data reduction. J Appl Crystallogr 45(2):324–328

19. de la Peña F, Ostasevicius T, Fauske VT, Burdet P, Jokubauskas P, Nord M, Sarahan M, Prestat E, Johnstone DN, Taillon J (2017) Electron microscopy (big and small) data analysis with the open source software package hyperspy. Microsc Microanal 23(S1):214–215

20. Clausen A, Weber D, Ruzaeva K, Migunov V, Baburajan A, Bahuleyan A, Caron J, Chandra R, Halder S, Nord M (2020) Libertem: Software platform for scalable multidimensional data processing in transmission electron microscopy. J Open Source Softw 5(50):2006

21. Thevenaz P, Ruttimann UE, Unser M (1998) A pyramid approach to subpixel registration based on intensity. IEEE Trans Image Process 7(1):27–41

22. Schindelin J, Arganda-Carreras I, Frise E, Kaynig V, Longair M, Pietzsch T, Preibisch S, Rueden C, Saalfeld S, Schmid B (2012) Fiji: an open-source platform for biological-image analysis. Nat Methods 9(7):676–682

23. Sundararaman M, Mukhopadhyay P (1993) Carbide precipitation in inconel 718. High Temp Mater Processes (London) 11(1–4):351–368

24. Ferreri NC, Vogel SC, Knezevic M (2020) Determining volume fractions of γ, γ', γ'', δ, and mc-carbide phases in inconel 718 as a function of its processing history using an advanced neutron diffraction procedure. Mater Sci Eng, A 781:139228

25. Li S, Wei Q, Shi Y, Zhu Z, Zhang D (2015) Microstructure characteristics of inconel 625 superalloy manufactured by selective laser melting. J Mater Sci Technol 31(9):946–952

26. Sui S, Tan H, Chen J, Zhong C, Li Z, Fan W, Gasser A, Huang W (2019) The influence of laves phases on the room temperature tensile properties of inconel 718 fabricated by powder feeding laser additive manufacturing. Acta Mater 164:413–427

27. Keller T, Lindwall G, Ghosh S, Ma L, Lane BM, Zhang F, Kattner UR, Lass EA, Heigel JC, Idell Y (2017) Application of finite element, phase-field, and calphad-based methods to additive manufacturing of ni-based superalloys. Acta Mater 139:244–253

28. Krakow R, Johnstone DN, Eggeman AS, Hünert D, Hardy MC, Rae CM, Midgley PA (2017) On the crystallography and composition of topologically close-packed phases in ati 718plus®. Acta Mater 130:271–280

29. Godec M, Malej S, Feizpour D, Donik Č, Balažic M, Klobčar D, Pambaguian L, Conradi M, Kocijan A (2021) Hybrid additive manufacturing of inconel 718 for future space applications. Mater Charact 172:110842

30. Šlapáková M, Zendegani A, Liebscher C, Hickel T, Neugebauer J, Hammerschmidt T, Ormeci A, Grin J, Dehm G, Kumar KS (2020) Atomic scale configuration of planar defects in the Nb-rich C14 Laves phase $NbFe_2$. Acta Mater 183:362–376

31. Gallmeyer TG, Moorthy S, Kappes BB, Mills MJ, Amin-Ahmadi B, Stebner AP (2020) Knowledge of process-structure-property relationships to engineer better heat treatments for laser powder bed fusion additive manufactured inconel 718. Addit Manuf 31:100977

32. Mantri SA, Dasari S, Sharma A, Alam T, Pantawane MV, Pole M, Sharma S, Dahotre NB, Banerjee R, Banerjee S (2021) Effect of micro-segregation of alloying elements on the precipitation behaviour in laser surface engineered alloy 718. Acta Mater 210:116844

33. Zhang F, Ilavsky J, Lindwall G, Stoudt MR, Levine LE, Allen AJ (2021) Solid-state transformation of an additive manufactured inconel 625 alloy at 700° c. Appl Sci 11(18):8643

34. Lindwall G, Campbell C, Lass E, Zhang F, Stoudt MR, Allen AJ, Levine LE (2019) Simulation of ttt curves for additively manufactured inconel 625. Metall Mater Trans A 50:457–467

35. Laleh M, Sadeghi E, Revilla RI, Chao Q, Haghdadi N, Hughes AE, Xu W, De Graeve I, Qian M, Gibson I (2022) Heat treatment for metal additive manufacturing. Prog Mater Sci 101051

36. Rafiei M, Mirzadeh H, Malekan M, Sohrabi MJ (2019) Homogenization kinetics of a typical nickel-based superalloy. J Alloy Compd 793:277–282

37. Fayed EM, Saadati M, Shahriari D, Brailovski V, Jahazi M, Medraj M (2021) Effect of homogenization and solution treatments time on the elevated-temperature mechanical behavior of inconel 718 fabricated by laser powder bed fusion. Sci Rep 11(1):2020

38. Xu L, Chai Z, Chen H, Zhang X, Xie J, Chen X (2021) Tailoring laves phase and mechanical properties of directed energy deposited inconel 718 thin-wall via a gradient laser power method. Mater Sci Eng A 824:141822

39. Ghaemifar S, Mirzadeh H (2023) Precipitation kinetics of niobium carbide (nbc) during homogenization heat treatment of additively manufactured inconel 718 superalloy. J Mater Res Technol

40. Mukherji D, Gilles R, Barbier B, Del Genovese D, Hasse B, Strunz P, Wroblewski T, Fuess H, Rösler J (2003) Lattice misfit measurement in inconel 706 containing coherent γ' and γ'' precipitates. Scripta Mater 48(4):333–339

41. Paulonis D, Oblak J, Duvall D (1969) Precipitation in nickel-base alloy 718. Pratt and Whitney Aircraft, Middletown, Conn
42. Yan S, Wang Y, Wang Q, Zhang C, Chen D, Cui G (2019) Enhancing mechanical properties of the spark plasma sintered inconel 718 alloy by controlling the nano-scale precipitations. Materials 12(20):3336
43. Zhang R, Qin H, Bi Z, Li J, Paul S, Lee T, Zhang S, Zhang J, Dong H (2020) Evolution of lattice spacing of gamma double prime precipitates during aging of polycrystalline ni-base superalloys: an in situ investigation. Metall Mater Trans A 51:574–585
44. Cozar R, Pineau A (1973) Morphology of y'and y" precipitates and thermal stability of inconel 718 type alloys. Metall Trans 4:47–59
45. Detor AJ, DiDomizio R, Sharghi-Moshtaghin R, Zhou N, Shi R, Wang Y, McAllister DP, Mills MJ (2018) Enabling large superalloy parts using compact coprecipitation of γ' and γ''. Metall Mater Trans A 49:708–717
46. Sriram H, Mukhopadhyay S, Kadirvel K, Shi R, Mills MJ, Wang Y (2023) Formation mechanisms of coprecipitates in inconel 718 superalloys. Acta Mater 249:118825

Publisher's Note Springer Nature remains neutral with regard to jurisdictional claims in published maps and institutional affiliations.